

# Aerodynamic Design of the Hyperloop Concept

Max M. J. Opgenoord\* and Philip C. Caplan†

Massachusetts Institute of Technology, Cambridge, Massachusetts 02139

DOI: 10.2514/1.J057103

The Hyperloop is a ground-based transportation system concept slated to drastically reduce travel times over medium range distances, for example between San Francisco and Los Angeles. This paper discusses aerodynamic design considerations for the Hyperloop pod. A Hyperloop capsule travels in an unconventional flow regime (very low Reynolds numbers with high Mach numbers), which brings with it unique challenges. This work focuses on the aerodynamic design of the Massachusetts Institute of Technology Hyperloop pod. For this design, it is crucial to delay separation over the pod as much as possible by forcing the boundary layer to transition farther upstream, resulting in a droplet shape for the aerodynamic shell. The performance of this design is investigated for nominal flow conditions as well as for flow conditions close to the Kantrowitz limit. The overall design of this team's Hyperloop pod won the design competition of the SpaceX Hyperloop Competition in January 2016.

## Nomenclature

$A$	=	reference area
$A_{\text{pod}}$	=	frontal area of pod
$A_{\text{tube}}$	=	cross-sectional area of tube
$C_D$	=	drag coefficient
$C_p$	=	pressure coefficient
$H$	=	shape parameter
$Kn$	=	Knudsen number
$l$	=	reference length
$M_{\text{ext}}$	=	external Mach number
$M_{\infty}$	=	freestream Mach number
$N_{\text{crit}}$	=	laminar instability amplitude exponent at which transition occurs
$P$	=	momentum defect
$p_{\text{tube}}$	=	tube ambient pressure
$Re$	=	Reynolds number
$Re_{\theta}$	=	Reynolds number based on momentum thickness
$t$	=	time
$\bar{t}$	=	nondimensional time
$u_e$	=	velocity at edge of boundary layer
$V_{\infty}$	=	freestream velocity
$y^+$	=	dimensionless wall distance
$\lambda$	=	Lamé parameter
$\rho_{\infty}$	=	freestream density
$\rho_e$	=	density at edge of boundary layer

## I. Introduction

THE Hyperloop is a concept for high-speed ground transportation, where passenger pods travel at transonic speeds in a partially evacuated tube. The concept was originally proposed in a white paper published by SpaceX in 2013 [1] as an alternative to the high-speed rail system currently being developed between Los Angeles and San Francisco, which was deemed too expensive and slow.

Presented as Paper 2017-3740 at the 35th AIAA Applied Aerodynamics Conference, Denver, CO, 5–9 June 2017; received 12 January 2018; revision received 29 May 2018; accepted for publication 3 June 2018; published online 28 July 2018. Copyright © 2018 by M. Opgenoord and P. Caplan. Published by the American Institute of Aeronautics and Astronautics, Inc., with permission. All requests for copying and permission to reprint should be submitted to CCC at [www.copyright.com](http://www.copyright.com); employ the ISSN 0001-1452 (print) or 1533-385X (online) to initiate your request. See also AIAA Rights and Permissions [www.aiaa.org/randp](http://www.aiaa.org/randp).

\*Team Lead and Aero/Structures Lead, Department of Aeronautics and Astronautics, MIT Hyperloop Team; [mopg@mit.edu](mailto:mopg@mit.edu). Student Member AIAA.

†Aero/Structures Engineer, Department of Aeronautics and Astronautics, MIT Hyperloop Team; [pcaplan@mit.edu](mailto:pcaplan@mit.edu). Student Member AIAA.

The Hyperloop concept could fill a growing need for an alternative transportation mode for short-haul travel. For short routes, such as Los Angeles–San Francisco or Boston–New York, the time spent traveling by aircraft at cruise speed is quite low compared to overall end-to-end travel time due to inescapable inefficiencies in air travel (runway taxiing, climb, descent, holding patterns, etc.). The high-frequency throughput of Hyperloop pods could alleviate some of these inefficiencies. Recently, KPMG published a preliminary study commissioned by Hyperloop One (one of the companies commercializing the Hyperloop concept) on the Helsinki–Stockholm corridor where they found that the Hyperloop could cut down end-to-end travel time by 75% to 28 min [2].

Momentum is growing in the Hyperloop movement, with a number of newly founded companies attempting to commercialize it. In addition, SpaceX is sponsoring a student competition to encourage innovation and to help accelerate the development of a working prototype, starting June 2015.<sup>‡</sup> Over 1000 teams submitted their intent to compete, and over 100 teams made it to design weekend in January 2016. The student team from the Massachusetts Institute of Technology (MIT) Hyperloop Team<sup>§</sup> won first place overall in that design weekend [3]. The aerodynamic design of that team's prototype is the subject of this paper.

Academic research into the Hyperloop concept has focused mostly on system integration. A conceptual sizing tool using the OpenMDAO framework [4] focuses primarily on the aerodynamic and thermodynamic interactions between the pod and tube, with recent work focusing on the energy consumption of the system [5]. The pods for the SpaceX Hyperloop Competition were the first physical prototypes of the Hyperloop concept. Recently, one team reported on their aerodynamic design [6]. For that design, a low-fidelity aerodynamic model was used to optimize the outer mold line, which was subsequently analyzed using a three-dimensional Reynolds-averaged Navier–Stokes solution with a turbulence model.

This paper describes the design approach for the aerodynamic shell used by the MIT Hyperloop Team. For rapid design iterations, we use an axisymmetric viscous/inviscid coupled boundary-layer method to accurately predict flow separation and transition. The final design is then analyzed using a three-dimensional computational fluid dynamics (CFD) solver, which is also used to characterize the aerodynamics at higher velocities to investigate the potential issues related to Hyperloop pods traveling through a partially evacuated tube at transonic speeds.

Section II discusses historic background of the Hyperloop concept as well as the SpaceX Hyperloop competition. Section III explains the design philosophy chosen by the MIT Hyperloop team as well as a brief overview of the overall pod design. Section IV then describes

<sup>‡</sup>Data available online at <http://www.spacex.com/hyperloop> [retrieved 05 February 2016].

<sup>§</sup>Data available online at <http://hyperloop.mit.edu> [retrieved 25 April 2017].

the aerodynamic design methodology. Section V focuses on the final aerodynamic design and its performance for different flow conditions.

## II. Background

The Hyperloop Alpha white paper [1] combined several historic concepts for magnetically levitating trains [7–9] and spurred a great deal of public interest in the concept, something that the earlier ideas were somewhat lacking. This white paper discusses a Hyperloop pod that travels at 1220 km/h in a partially evacuated tube (1/1000 of atmospheric pressure) levitating using air bearings. The use of wheels at these high speeds would be quite problematic because of the massive centripetal forces on them. Air bearings are proposed as a more efficient mechanism, where the pod floats on a thin film of compressed air. In the Hyperloop Alpha concept, this compressed air is supplied by an onboard compressor. Propulsion is provided by a linear induction motor. The benefit of this is that the heavy components are built track-side, and the pod only has to carry a rotor which makes the propulsion quite efficient. Furthermore, that same linear induction motor can also be used for braking at the other end of the tube to recover a substantial amount of energy.

The onboard compressor is also used to improve the efficiency of the pod at higher speeds. Once the pod reaches transonic speeds, the flow around the pod will start to choke (i.e., the flow around the pod will become sonic). At this sonic condition (the so-called Kantrowitz limit [10]), the mass flow around the pod is at its maximum. Therefore, when the speed is further increased, not all flow can travel around the pod and is therefore collected in front of the pod. The result is a column of air being pushed by the pod throughout its run. That pressure build-up results in significant additional drag. The Hyperloop Alpha concept therefore introduces the onboard compressor to compress the additional flow and suck it through the pod, while at the same time supplying compressed air to the air bearings.

Two years after publishing the Hyperloop Alpha white paper, SpaceX announced the Hyperloop student competition to advance the concepts proposed in that white paper to the next level, while at the same time garnering more interest from students, universities, and the general public for the concept. In this competition, students are to design and build Hyperloop pods, which are then tested on a 1-mile-long, 6-ft-diam tube built by SpaceX. The tube has a flat concrete base on which aluminum (Al 6101) track plates and an aluminum I-beam are installed.

The competition is intentionally kept very open, allowing for a variety of different designs. Taking the levitation concepts as an example, wheels, air bearings, and magnetic levitation are all allowed. The Hyperloop Alpha concept used a linear induction motor to get up to speed. However, such a system requires a great deal of integration between the pod and track. With more than 20 teams competing, managing such a tight integration between the track and many diverse pods is quite hard to handle. Therefore, SpaceX provides a pusher vehicle to bring pods up to speed. This pusher vehicle is a stripped-down Tesla vehicle that can accelerate a 250 kg pod at 2.4g.

The most important scoring criteria for the competition are the overall run time (therefore favoring high cruise speeds and fast braking) and the potential to scale up the technologies used in the competition vehicle to a full-scale Hyperloop vehicle. Competition rules were released in August 2015, with competition weekend taking place in summer 2016,<sup>†</sup> in which teams would compete against one another with their finished prototypes. The competition was therefore on a tight timeline, leading to compressed design and production phases. The competition is described in more detail by Opgenoord et al. [11].

## III. Overall Pod Design

The competition goal is to advance the Hyperloop concept to the next level by designing technologies that one day could be used in full-scale Hyperloop and by using these technologies in a working Hyperloop prototype. Here, we cover the final top-level design of the MIT Hyperloop pod. A more detailed overview is provided in [11].

The overall goal of the MIT Hyperloop Team within this competition was to design and build a pod that scores well in both aspects of the competition (i.e., speed and scalability of systems used). The speed goal favors a lightweight design, whereas the scalability goal comes back in every aspect of the pod. There are several approaches that could be taken to design for scalability, for instance to design a full Hyperloop pod with a large passenger compartment and scale it down for the competition. The MIT Hyperloop team took the approach of focusing on the most important technologies for the Hyperloop concept and developing scalable technologies for those. Therefore, a major focus was the scalability of the levitation design, the braking design, and the aerodynamics.

Other major driving requirements for the design were imposed by the team itself. First, the pod had to be built in four months (February 2016 start of manufacturing to May 2016 fully assembled), which meant that simpler/easier-to-manufacture designs were often favored. Second, the pod needed to accelerate at 2.4g, the maximum proposed acceleration offered by the SpaceX pusher. Finally, the pod had to be robust to changes in performance specifications and track tolerances.

An overview of the MIT Hyperloop design is shown in Fig. 1. The prototype is 2.4 m long, weighs 258 kg, and is designed for a top speed of 400 km/h. The pod has no propulsion onboard because we rely on the SpaceX pusher to get up to cruising speed.

Passive magnetic levitation is used to levitate above the track; specifically, the pod uses an electrodynamic suspension (EDS) system. Although the original Hyperloop Alpha concept uses air bearings, the track tolerances were poor enough that a large pressure vessel would be required to keep sufficient track clearance (greater than 2 mm), and it was therefore decided not to use air bearings. EDS works with larger gap heights (on the order of a few millimeters), and additionally becomes more efficient at higher speeds. The levitation system does not require power; therefore, it scores well for scalability because of its safety and efficiency at high speeds. Electrodynamic suspension systems are notorious for being highly underdamped and sometimes even unstable [12,13]; therefore, a suspension is added between the magnet arrays and the pod.

The eddy-current braking system uses the same physical principle as the levitation design, only now the design is optimized for drag rather than lift. The design is similar to an eddy-current brake on a rollercoaster. As discussed earlier, linear induction motors will likely be the best technology for propulsion and deceleration. However, track-side infrastructure is required for that. In the case of an anomaly midrun (e.g., a problem with a pod farther down the track, tube depressurization/breach, etc.), the pod still has to brake. Therefore, the braking system on the MIT Hyperloop pod is designed as an emergency braking system for a full-scale Hyperloop, decelerating the pod upward of 2.4g.

The pod does not have an onboard compressor, both because of the lower speeds in the competition and because the pod does not have air bearings that need to be supplied with air. The Kantrowitz limit will be further discussed in Sec. V.

## IV. Aerodynamic Design Methodology

This section details the design approach used for the aerodynamic shell and discusses any analysis tools used in the design.

### A. Requirements

The main performance requirement for the aerodynamic shell is to keep the overall  $C_D A^{**}$  for the pod below 0.5, to adhere to the overall

<sup>†</sup>This eventually got pushed to January 2017.

<sup>\*\*</sup>We focus on  $C_D A$  comparisons instead of just  $C_D$  comparisons because tweaks in the geometry can result in different frontal areas between designs, which would invalidate any comparison of  $C_D$ .

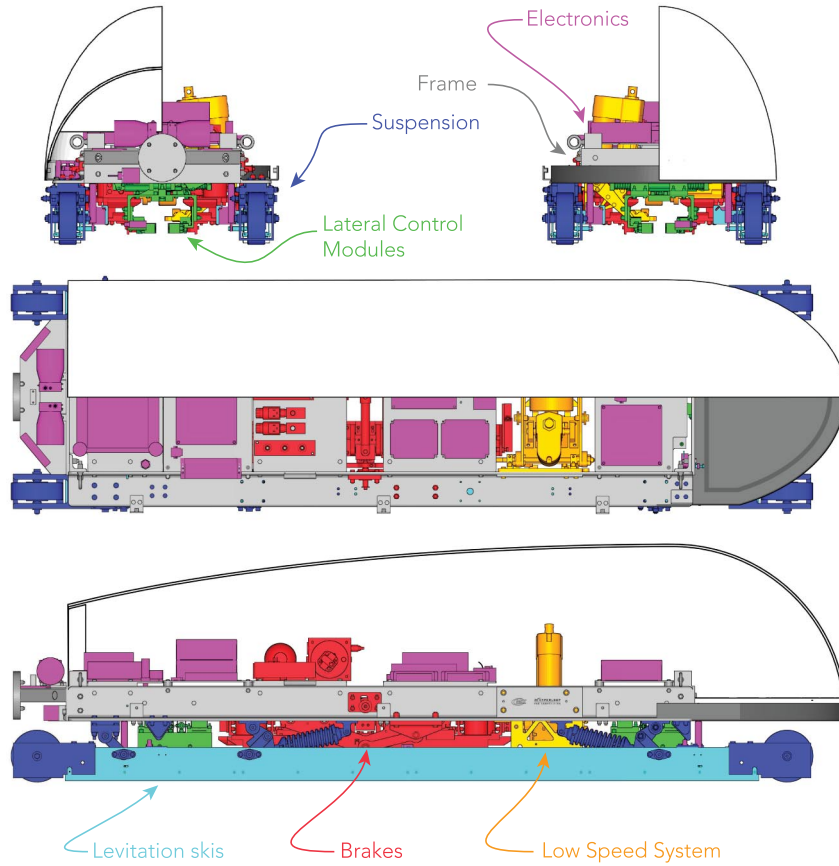


Fig. 1 Overview of the MIT Hyperloop design.

pod run time requirement.  $C_D$  is the drag coefficient, and  $A$  is the reference area, in this case the pod frontal area. Furthermore, the rules require that a dummy is carried in the pod “in a reasonable position” during the test. We chose to use a 3 ft dummy. Other self-imposed requirements are to keep the total weight of any aerodynamic covers below 10 kg and to be able to access the inside of the pod within 2 min.

Of course, the aerodynamic shell has to cover the structural frame, while leaving enough room for the dummy, electronics, hydraulics, etc., inside the pod, as shown in Fig. 1. In this case, the other subsystems drive the size of the shell.

## B. Flow Regime

The choice of analysis tools for the aerodynamics of this pod depends strongly on the flow regime the pod experiences. Even though a Hyperloop pod operates in a large partially evacuated tube, the remaining air in the tube still necessitates a careful aerodynamic design of the outer shape of the pod. Therefore, the MIT Hyperloop pod has an aerodynamic shell to cover the internals of the pod. To reduce manufacturing risk, the aerodynamic shell is decoupled from the structural frame of the pod, motivated by the aggressive manufacturing timeline in this project.

A Hyperloop pod operates in an unconventional flow regime, as it travels at high speed through a partially evacuated tube. For the SpaceX Hyperloop competition, the tube pressure is 860 Pa, and the pod will travel at 250 mph. Even though the pressure is quite low, the fluid can still be modeled as a continuum. The Knudsen number  $Kn$  is a dimensionless parameter that is typically used to describe the boundary of continuum flow and is defined as the ratio between the molecular mean free path  $\lambda$  and a characteristic length scale in the flow [14]. For this flow condition, the Knudsen number is  $Kn = \mathcal{O}(10^{-6})$ , which is still well below the  $\mathcal{O}(10^{-1})$  continuum limit [15].

The Reynolds number for this flow regime is around 60,000,<sup>††</sup> which means that the flow will transition from laminar to turbulent

flow somewhere on the pod. Capturing this transition accurately is crucial and therefore drives the selection of appropriate aerodynamic analysis tools. This Reynolds number is of the same order of magnitude as the full-scale Hyperloop pod in the Hyperloop Alpha paper, which travels at a higher speed and is longer, but the pressure in the tube is 10 times lower. Finally, the Mach number for the SpaceX Hyperloop competition is around 0.3, requiring compressibility of the fluid to be taken into account. For a full-scale Hyperloop at higher speeds, this Mach number is considerably higher.

As mentioned earlier, the Kantrowitz limit is not significant for this competition due to the lower speeds, and therefore no compressor is included in design analyses.

## C. Flow Analysis

During the preliminary design phase, extensive flow analyses are carried out to characterize the design space. Relying on a three-dimensional (3-D) Navier–Stokes CFD simulation for each design tweak was deemed too expensive. In the compressed design cycle of this project, it was considered more appropriate to evaluate thousands of designs using a cheaper model and only use a 3-D Navier–Stokes CFD simulations in the final stages of the design phase. Therefore, in the preliminary design phase, we relied on an axisymmetric viscous/inviscid analysis code, MTFLOW [16]. Moreover, this viscous/inviscid analysis code allows for capturing transition of the boundary layer from laminar to turbulent accurately, which is critical to the design. MTFLOW is typically used to design axisymmetric bodies and axisymmetric flow passages. This throughflow code uses an integral boundary-layer method to solve for the laminar or turbulent boundary layer and a streamline curvature formulation to solve for the inviscid outer flow. The coupling between the inviscid and viscous flow is achieved through the displacement body model. MTFLOW uses the  $e^n$  method to capture boundary-layer transition [17,18]. We used MTFLOW v2.12, which improves its accuracy for geometries with blunt trailing edges.

To analyze the final 3-D shape of the pod, we resorted to a 3-D Navier–Stokes solver. Unfortunately, these solvers in general are

<sup>††</sup>The pod’s length is used as the characteristic length throughout this paper.

worse at capturing transition than a viscous/inviscid analysis code like MTFLOW, which is another reason to use MTFLOW to capture Reynolds number effects or small tweaks in the geometry.

#### D. Geometry

To facilitate rapid design iterations, we parameterize the aerodynamic shell in terms of a few geometric parameters, which can be used for tradeoff studies. The curvatures in the geometry are generated using Lamé curves (also known as superellipses) [19]. The geometry for the aerodynamic shell as shown in Fig. 2 is parameterized in terms of the overall length of the pod, nose length  $l_n$ , width of the pod  $w$ , height of the nose  $h_n$ , tail height  $h_t$ , and the Lamé parameters for the nose  $\lambda_n$ , the side of the nose  $\lambda_{sn}$ , the back  $\lambda_b$ , and the side of the back  $\lambda_{sb}$ .

The geometry shown in Fig. 2 is a three-dimensional geometry, whereas for preliminary design studies, we rely on an axisymmetric solver. The conversion from such a three-dimensional geometry to an axisymmetric one is never perfect. For one, the pod actually does not travel in the middle of the tube but travels toward the bottom of the tube. The tube is also not perfectly circular because of the concrete base. However, by using a variable axisymmetric tube radius, we can minimize the discrepancies between the axisymmetric and three-dimensional geometries. The variable axisymmetric tube radius is

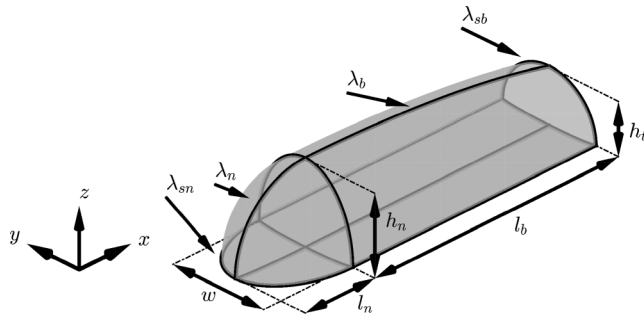


Fig. 2 Design parameters for shell geometry.

chosen such that the area ratio between the axisymmetric tube and axisymmetric pod is the same as the area ratio between the actual tube and three-dimensional pod. This process is illustrated in Fig. 3. For the axisymmetric shape, we revolve the top centerline of the outer mold line on itself.

### V. Pod Aerodynamic Design

The main tradeoffs for the aerodynamic design of the MIT Hyperloop pod are discussed in this section. We discuss the final aerodynamic shape and its performance at competition speeds, and we characterize its performance at transonic speeds.

#### A. Kantrowitz Limit Considerations

When a pod travels at transonic speeds through a tube, it could choke the flow around the pod. This happens when the Mach number of the flow around the pod is equal to 1. When the pod speeds up further, a large pressure increase in front of the pod results because the mass flow that can go around the pod is limited. This sonic condition is known as the Kantrowitz limit [10]. There are two main ways to avoid the Kantrowitz limit. The first option is to increase the ratio between tube cross-sectional area and pod cross-sectional area, thereby allowing relatively more air to pass around the pod at a lower velocity. The other option uses a compressor that sucks in air through the front of the pod and feeds the compressed air through a duct in the pod which subsequently exits through a nozzle at the back, which is the approach taken in the Hyperloop Alpha white paper [1]. Neither option is perfect; it means either limiting the cross-sectional area of the pod, hence decreasing payload or increasing tube construction costs, or adding an expensive, high-maintenance compressor to each pod. Furthermore, transonic compressors at such low Reynolds numbers would require a large research and development effort because they are not in use in any aerospace application today.

As shown in Fig. 1, the pod does not have a compressor because it is not worthwhile to use one for the SpaceX Hyperloop competition. Figure 4 shows the variation of the external Mach number to the pod-to-tube ratio and the freestream Mach number. The external Mach

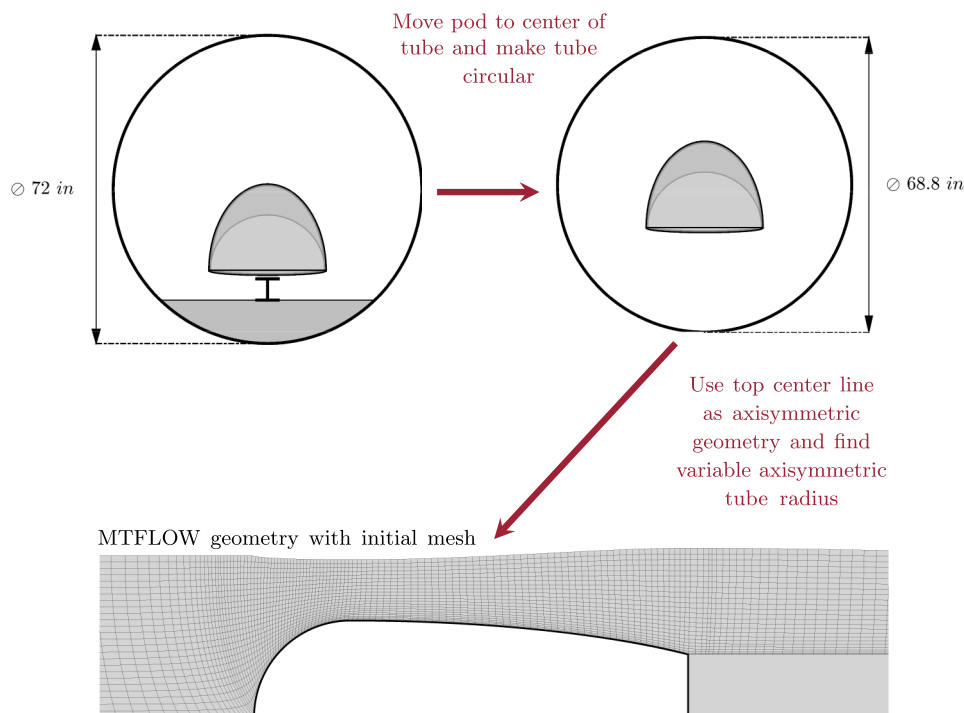
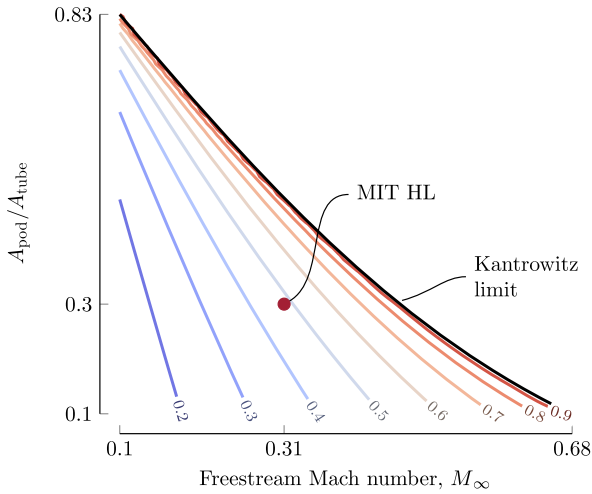


Fig. 3 Illustration of recovering the axisymmetric geometry from the full three-dimensional geometry.





**Fig. 4 Area ratio (pod-to-tube) vs freestream Mach number. The contour lines indicate  $M_{\text{ext}}$ .**

number  $M_{\text{ext}}$  is the maximum Mach number of the flow around the pod. The flow is choked when the external Mach number equals 1.0. Figure 4 clearly shows that, for a reasonably sized pod without a compressor, the Kantrowitz limits the speed of the pod without an additional drag increase. At an area ratio of 0.3 and a Mach number of 0.31, the flow around the pod is not even close to choking, as seen in Fig. 4. Because compressors also have a large risk associated with them in terms of design, manufacturing, and cost, the MIT Hyperloop team decided not to use a compressor.

## B. Axisymmetric Design

First, an axisymmetric aerodynamic shell was designed using MTFLOW [16]. All of the results in this section are generated using MTFLOW. In the aerodynamic design, we relied on sweeps over the design parameters in Fig. 2, rather than going for a purely numerical optimization method. The main reason for this was to gain more physical insight in this design problem with a large unexplored design space and to use constraints that would be harder to capture in mathematical statements. Additionally, this allowed for a more aggressive design schedule.

At these low Reynolds numbers ( $Re \approx 60,000$ ), the boundary layer separates very easily, and proper aerodynamic design is needed to reduce that as much as possible to keep the pressure drag to a minimum. As an example, consider the sleek axisymmetric shape in Fig. 5. The laminar boundary layer separates at a very low adverse pressure gradient (just after the inflection point on the geometry), and therefore this shape results in large amounts of pressure drag. Thus, even though the skin friction drag is low due to laminar flow existing on the surface, the pressure drag is high because of the large wake. This laminar separation has to be prevented to reduce drag. Turbulent boundary layers can handle larger pressure gradients, and a key part to this aerodynamic design is therefore to ensure that the boundary layer transitions to turbulent toward the nose of the pod.

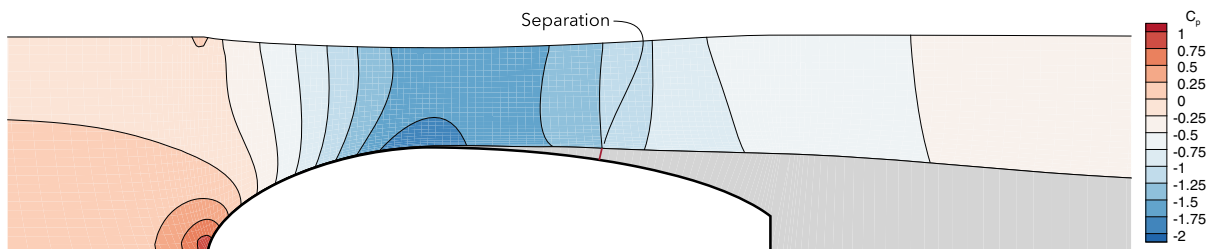


**Fig. 5 Laminar flow separation on a Hyperloop pod at a Reynolds number  $Re = 60,000$  and Mach number  $M_{\infty} = 0.3$ . The boundary layer and wake are indicated in gray.**

The transition location depends on  $N_{\text{crit}}$ , which is a measure for the ambient disturbance level as well as some degree of receptivity [20]. Because we expect the environment in the tube to be fairly noisy (e.g., dust in the tube or vibrations due to track disturbances), we use  $N_{\text{crit}} = 4$  throughout the design. This value for  $N_{\text{crit}} = 4$  corresponds to the same turbulence levels as in a high-turbulence wind tunnel.

In the following, several key design parameters and key parts of the design process are highlighted, focusing on the dummy position, nose shape, tail height, and the effectiveness of an aerodynamic tail. The final axisymmetric design is also discussed as well as its sensitivity to Reynolds number and tube pressure.

### 1. Dummy Position

The dummy is the largest “component” that has to be fit inside the shell, and its position is therefore an important consideration in the design of the aerodynamic shell. Here, we show the tradeoff between two options. The first option is to put the dummy in the nose of the pod in an upright position, thereby leaving more room for components toward the rear of the pod but resulting in a higher nose. The second option is to lay the dummy more flat over the components inside the pod, thereby reducing the height of the pod and allowing for a more gradual ramp-up to the highest point of the pod.

Figure 6 shows the results for both of these shapes. The momentum defect  $P$  shows where on the pod the drag is built up, as the value of  $P$  far downstream directly corresponds to the drag. The momentum defect is defined as  $P = \rho_e u_e \theta$ , where  $\rho_e$  and  $u_e$  are the density and velocity at the edge of the boundary layer, respectively, and  $\theta$  is the momentum thickness. The shape parameter  $H$  is the ratio of displacement thickness to momentum thickness, and it is a measure for the shape of the boundary layer [20].

As Fig. 6 shows, for the shape with the dummy in the nose, the boundary layer transitions much closer to the nose, therefore delaying separation and reducing pressure drag. For the shape with the dummy laying flat, the laminar boundary layer separates close to the highest point on the pod, resulting in large pressure drag. Therefore, even though the shape with the dummy in the nose has a larger cross-sectional area, the drag is lower. The reason for this is the blunt nose, which is known to promote early transition [21].

### 2. Nose Shape and Tail Height

Figure 7 shows the influence of the nose Lamé parameter and the tail height on the drag coefficient. When the nose is too shallow (e.g.,  $\lambda_n = 1.5$ ), transition will occur later on the pod, and more pressure drag results. However, too blunt of a nose increases the curvature on the highest point of the nose, which also induces separation. For the tail height, a larger tail height increases the pressure drag. However, decreasing the tail height too much is not beneficial because then the flow separates early, again leading to a pressure drag increase. The geometric constraints induced by the packaging of the pod components allowed for the lowest tail height without further causing the separation point to move forward.

### 3. Aerodynamic Tail

An aerodynamic tail section is sometimes used to reduce the drag of bluff bodies. The idea is to keep a straight section of most of the

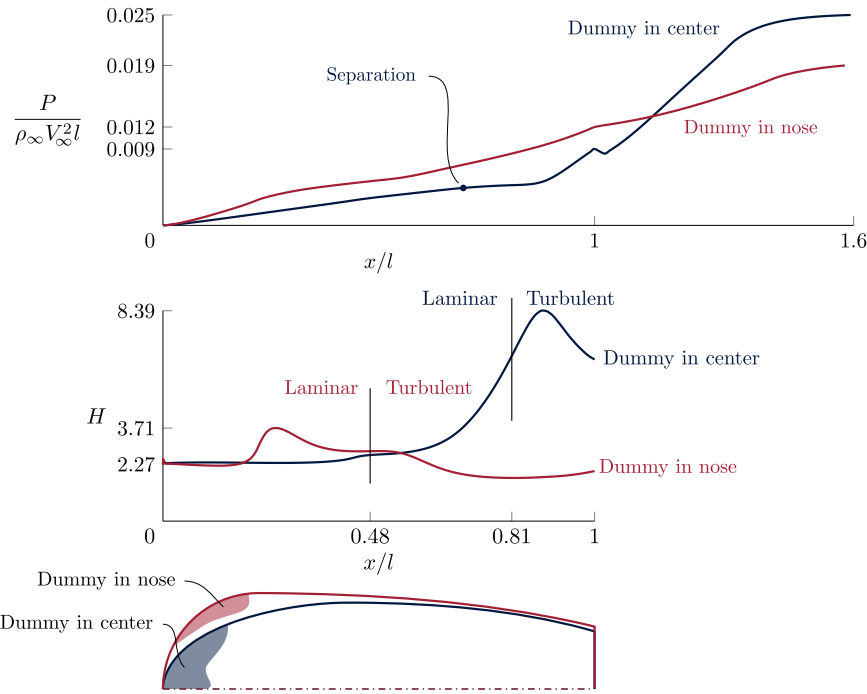
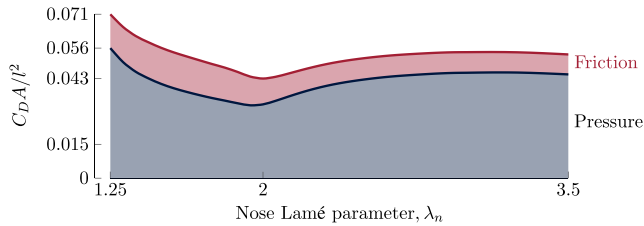
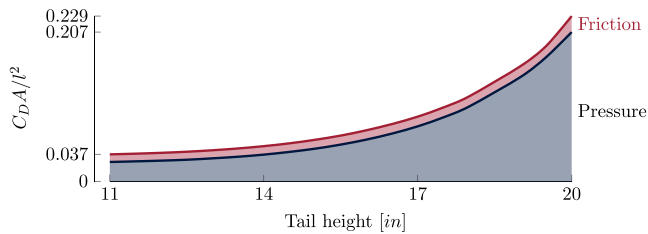


**Fig. 6** Shape parameter and momentum defect for different dummy positions: one with the dummy in the center ( $C_D A/l^2 = 0.0553$ ), one with the dummy in the nose ( $C_D A/l^2 = 0.0431$ ).



**a) Nose bluntness influence on  $C_D A$  for tail height of 12 in**



**b) Tail height influence on  $C_D A$  for nose Lamé parameter  $\lambda_n = 2.0$**

**Fig. 7** Nose bluntness and tail height influence on drag for axisymmetric pod.

components on the pod to provide maximum payload capacity and then add a lightweight aerodynamic tail section to keep drag to a minimum. We compare such a design to our final design in Fig. 8. The concept with an aerodynamic tail has a smaller cross-sectional diameter to keep the internal volume (excluding tail) similar. The momentum defect on the pod surface is lower for the pod with an aerodynamic tail because there is no adverse pressure gradient on the pod. However, the flow separates as soon as the aerodynamic tail is reached, dramatically increasing the momentum defect. Even when the flow is tripped ahead of the aerodynamic tail (see dashed line in Fig. 8), the flow separates quickly after the start of the aerodynamic tail, still resulting in a large momentum defect. The large increase in pressure drag therefore renders the aerodynamic tail ineffective.

#### 4. Final Axisymmetric Geometry

The flowfield around the final geometry is shown in Fig. 9. As mentioned several times, if we can delay separation, we can dramatically reduce the pressure drag because a turbulent boundary layer can handle adverse pressure gradients better. Therefore, the final design has a blunt nose section, which triggers transition slightly downstream of the tallest point of the pod. This results in attached flow at the very back of the pod. The back of the pod is not tapered down further because trying to close it completely (i.e., such that the cross-sectional area of the back is 0) is futile because the flow would separate anyway. Additionally, this shape results in clean separation off the back of the pod, which aids stability, although this is less of a problem here because the ratio of aerodynamic forces to inertial forces on the pod is quite low.

#### 5. Sensitivity to Reynolds Number and Tube Pressure

As shown in Fig. 10a, the variation of drag as a function of Reynolds number is similar to the well-known variation of drag over a cylinder as a function of Reynolds number [22]. The results for low-turbulence freestream are computed with  $N_{crit} = 7.0$  to compare the influence of surface roughness (characterized by  $N_{crit}$ ). We see that this roughness is quite important for the drag of the pod in Fig. 10. Trying to trip the boundary layer near the nose could therefore be helpful. This could be achieved by roughening up the nose section. However,  $Re_\theta$  may not be high enough to effectively use a physical trip on the nose section.  $Re_\theta$  is the Reynolds number based on the momentum thickness of the boundary layer. For a flat plate, transition from laminar to turbulent flow is only possible when locally  $Re_\theta \gtrsim 160$  [23]. The  $Re_\theta$  variation over the pod is shown in Fig. 11 for the final design, where the critical  $Re_\theta$  occurs after free transition. In the end, we decided against tripping the boundary layer because this would require detailed wind-tunnel experiments to get right, and the team would rather spend those valuable resources elsewhere.

#### C. Final Three-Dimensional Shape

To generate the three-dimensional shape from the final axisymmetric shape, the axisymmetric shape is used as the centerline for the pod. The other design parameters from Fig. 2 are determined

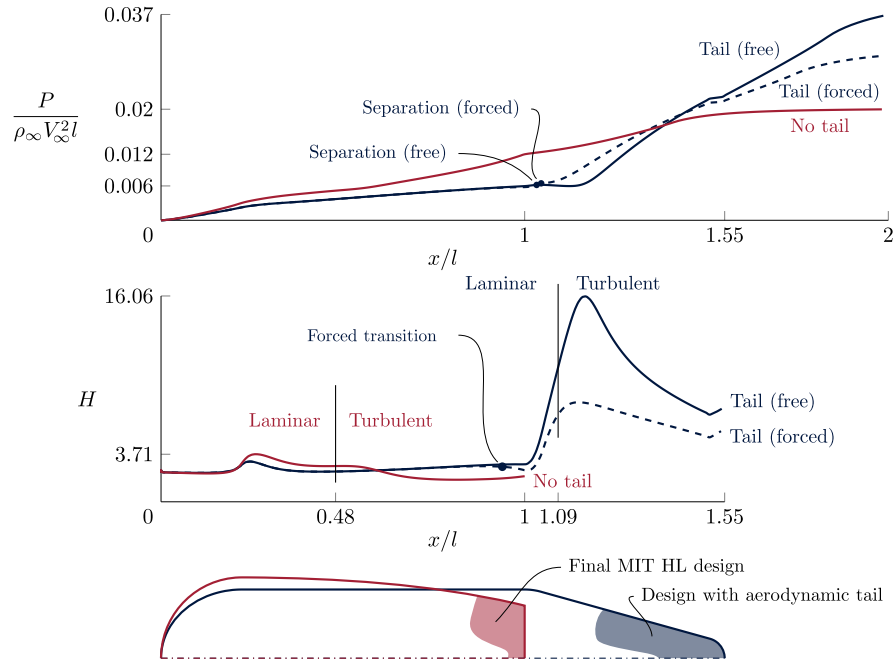


Fig. 8 Comparison between designs with aerodynamic tail ( $C_D A/l^2 = 0.0950$ ) and without aerodynamic tail ( $C_D A/l^2 = 0.0431$ ).

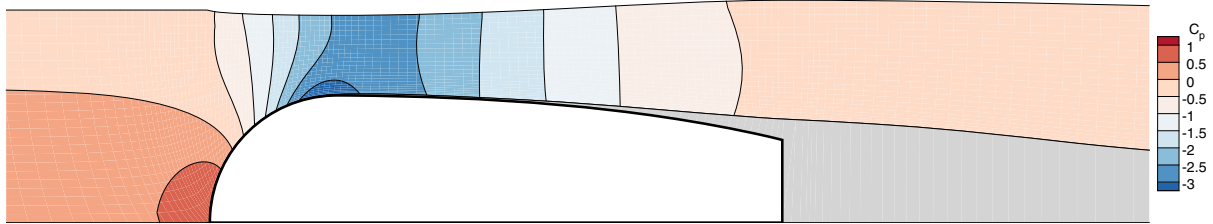


Fig. 9 Flowfield around the final axisymmetric design at Reynolds number  $Re = 60,000$  and Mach number  $M_\infty = 0.3$ . The boundary layer and wake are indicated in gray.

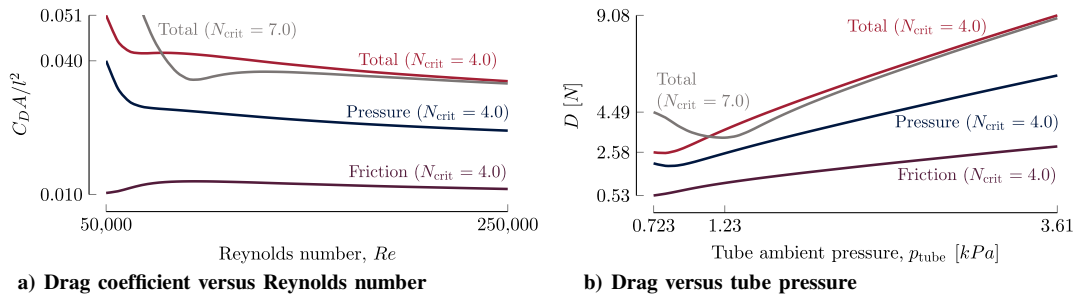


Fig. 10 Sensitivity of final axisymmetric shape to Reynolds number and tube pressure. In Fig. 10b, the tube pressure is proportional to Reynolds number because the pod velocity and tube temperature are kept constant.

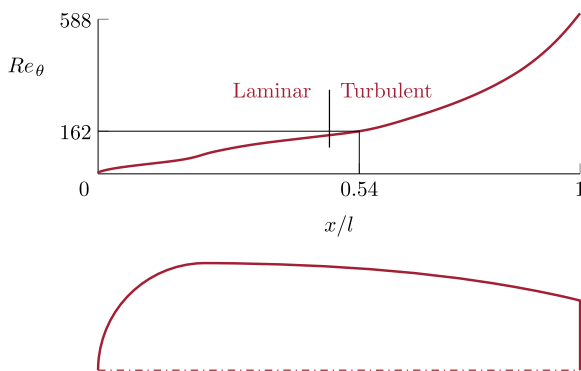
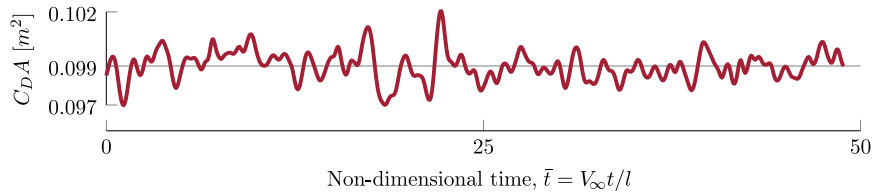
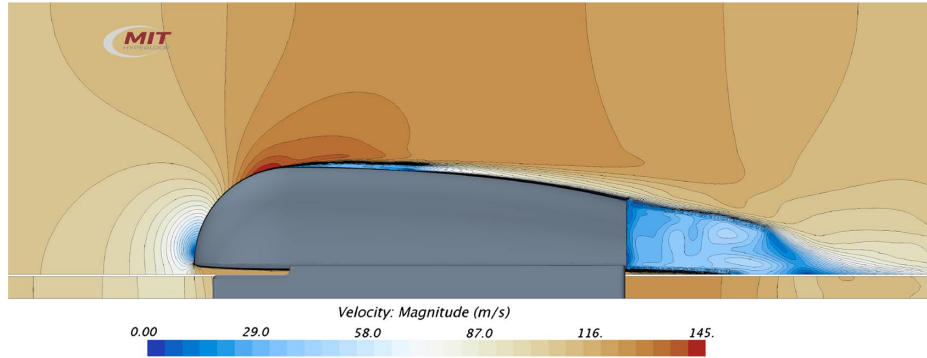


Fig. 11  $Re_\theta$  vs  $(x/l)$  for the final pod design.

from packaging constraints with the other subsystems (e.g., structural frame, electronics, hydraulics, etc.). We study the performance of this design using STAR-CCM+. For these simulations, we solve the laminar Navier–Stokes equations on a very fine grid (2.58 million cells), with the grid extending 25 pod lengths in front and 30 pod lengths to the back. A laminar solution could overestimate flow separation, thereby leading to conservative drag values. However, adding a turbulence model would overestimate the transition location to be too far upstream and therefore underestimate separation to occur too far downstream. Using a fixed transition location for the turbulence model could also be used, but it is unknown what the transition location is for the sides of the pod because these regions deviate significantly from the axisymmetric shape. These simulations have to be unsteady because flow separation off the back is an inherently unsteady phenomenon. Total flow conditions (total temperature, total pressure)



a) Drag coefficient versus non-dimensional time  $\bar{t}$



b) Velocity field contours at  $\bar{t} = 48$

**Fig. 12** Laminar Navier–Stokes solution of the final aerodynamic design at  $V_\infty = 110$  m/s ( $Re = 60,000$ ,  $M_\infty = 0.32$ ).

are set at the inlet to the domain, and a pressure outlet is used at the outflow.

The results for the laminar Navier–Stokes simulations over the pod are shown in Fig. 12. We can see a small degree of vortex shedding off the back of the pod, but the overall influence on the drag coefficient is low, as shown in Fig. 12a. Vortex shedding is to be expected at these low Reynolds numbers [24]. The drag coefficient is, of course, quite different from the axisymmetric case due to 3-D interference effects. We see that the flow over the top of the pod stays attached until the back, except for a small laminar separation zone just behind the tallest point. This agrees with the axisymmetric results (Fig. 6), in which there also is a laminar separation bubble just behind the tallest point of the pod. The drag could be lowered by covering the skis with aerodynamic covers. However, this would reduce accessibility to critical components on the skis, and therefore no aerodynamic covers for the skis are used.

#### D. Performance at Transonic Speed

Although the pod will not see any transonic speeds during the competition, we still investigate its performance at higher speeds here because it is such an important part of the Hyperloop concept. In this part of the work, we rely on turbulent 3-D Navier–Stokes simulations. At these higher speeds (we increase the pod velocity, thereby increasing both Mach number and Reynolds number for the same tube pressure), turbulent flow is expected over a larger portion of the pod, and therefore using a turbulence model is more justified. We use the  $\kappa\text{-}\omega$  shear-stress transport turbulence model [25,26], which is known for handling separated flows and adverse pressure gradients well [27].

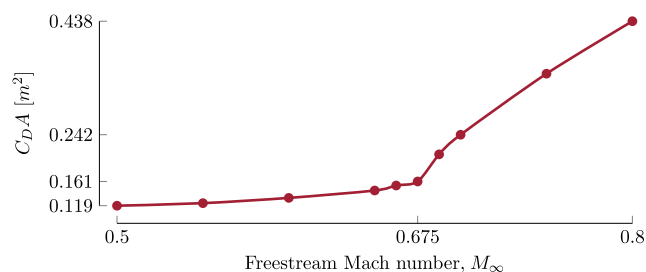


**Fig. 13**  $C_D A$  vs Mach number for the final design. The large drag build-up starts around  $M_\infty = 0.675$ .

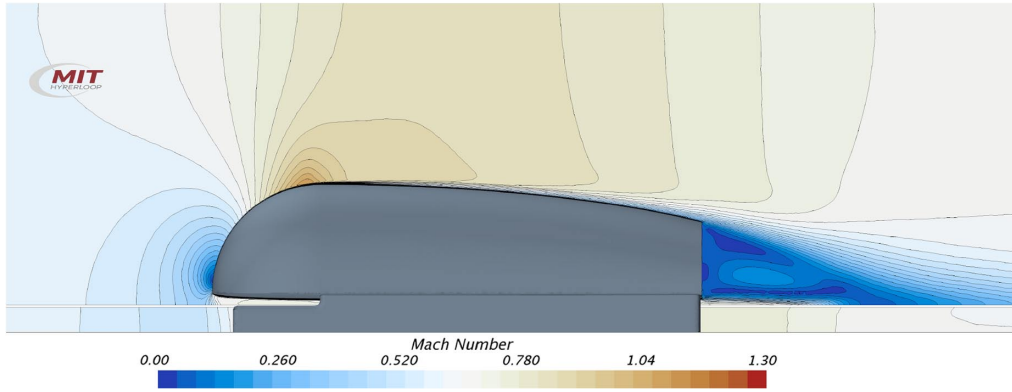
Any simulation near and above the Kantrowitz limit has to be unsteady. The choking of the flow around the pod and the subsequent pressure build-up is an inherently unsteady phenomenon, and it prevents a steady simulation from converging. This also requires careful setup of the inlet and outlet boundary conditions (i.e., specifying total pressure and temperature at the inlet and a pressure outlet at the outflow boundary). Note that the meshes for each run are different to ensure that  $y^+ \leq 1$  everywhere on the pod boundary.

The change in  $C_D A$  as a function of Mach number is shown in Fig. 13. Note that the freestream density and temperature are kept constant; therefore, the Reynolds number increases proportionally with Mach number. The small drag increase from  $M_\infty = 0.5$  to  $M_\infty = 0.65$  can be explained by the flow turning supersonic over the highest point of the pod (as shown in Fig. 14a), which results in a small shock with associated wave drag. Although part of the flow over the pod is supersonic at those freestream Mach numbers, the flow has not choked yet because the supersonic region does not reach all the way to the tube boundaries. The flow around the pod chokes around  $M_\infty = 0.675$ , resulting in a large drag increase for larger Mach numbers. Because of the fact that not all flow can continue past the pod, a pressure build-up in front of the pod results. Figure 15 shows the pressure coefficient along the tube, 1 m above the pod, which clearly shows a large pressure increase in front of the pod for freestream Mach numbers higher than 0.675. The drag build-up due to exceeding the Kantrowitz limit is significant; the drag coefficient is three times as high for  $M_\infty = 0.8$  compared to  $M_\infty = 0.65$ . Note that part of the drag increase is also the result of the wave drag increase due to the associated strong normal shock, as shown in Fig. 14c. Furthermore, the shock-induced boundary-layer separation for  $M_\infty > 0.70$  also increases the pressure drag.

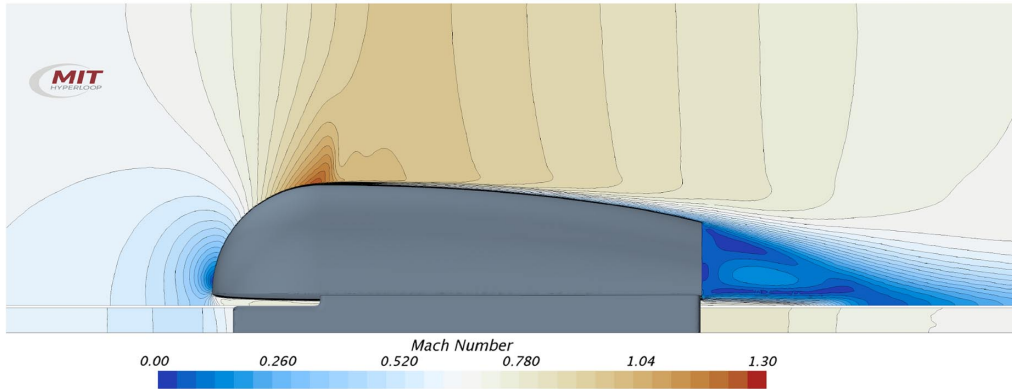
The threefold drag increase due to exceeding the Kantrowitz limit results in a power loss of 31 kW. However, it is questionable that a compressor used to avoid exceeding the Kantrowitz limit would use less power. For example, the Hyperloop Alpha concept's first-stage compressor has a power requirement of 276 kW [1], and Chin et al. found that, for their configuration, the compressor power requirement exceeded 300 kW [4]. For our configuration, if we assume an isentropic efficiency for the compressor of 80% and a duct<sup>††</sup> area of 0.05 m<sup>2</sup>, the power requirement for the compressor is 204 kW at

<sup>††</sup>The duct feeds the compressed air from the compressor outlet to the nozzle at the back of the pod.

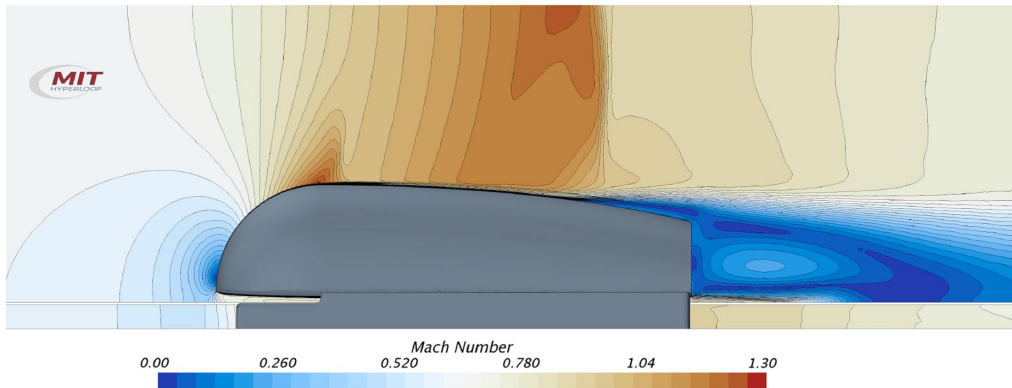




a)  $M_\infty = 0.65$  ( $Re = 293,000$ ), below Kantrowitz limit



b)  $M_\infty = 0.675$  ( $Re = 304,000$ ), below Kantrowitz limit, a small shock develops



c)  $M_\infty = 0.70$  ( $Re = 316,000$ ), above Kantrowitz limit

Fig. 14 Contours of local Mach number around the pod for different freestream Mach numbers.

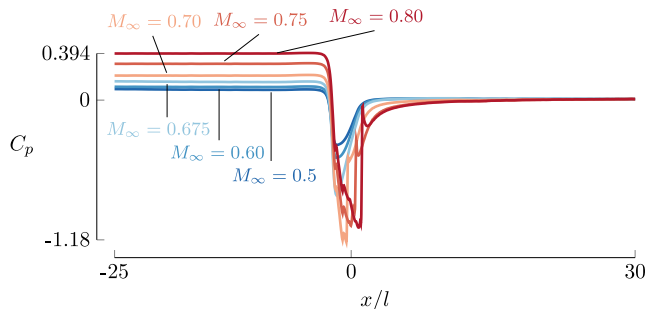


Fig. 15 Pressure coefficient at 1 m above the base of the shell along tube for different Mach numbers.

$M_\infty = 0.80$ . Of course, if the power requirement for a compressor to avoid the Kantrowitz limit is higher than the power loss due to the additional drag from exceeding the Kantrowitz limit, adding a compressor would be futile.

## VI. Conclusions

This paper presented the aerodynamic design of the MIT Hyperloop pod, which participated in the SpaceX Hyperloop Competition from 2015 to 2017, where it won best overall design at design weekend in January 2016. Note that this design study focused on the aerodynamic design for this competition; for a full design study, other factors need to be taken into account, such as packaging of passenger compartments, performance through corners, etc.

The aerodynamic design strategy was twofold. First, geometry sweeps were performed using a fast axisymmetric viscous/inviscid analysis tool, while accounting for different flow rates between the axisymmetric and 3-D shape. In the aerodynamic design, it was crucial to transition the boundary layer to turbulent close to the front of the pod such that higher adverse pressure gradients are tolerated before separation. Such a design strategy increases friction drag but dramatically reduces pressure drag. Once the axisymmetric shape was decided upon, the final three-dimensional geometry was analyzed using a three-dimensional Navier-Stokes solver to characterize its final performance at design speed.

Concluding, for the aerodynamic flow regime for this SpaceX Hyperloop Pod Competition, a droplet shaped aerodynamic shell is most effective at delaying flow separation, lowering the drag substantially. By investigating the performance of the design at transonic speed, it was also found that violating the Kantrowitz limit could lead to threefold increase in drag coefficient for an increase in Mach number from 0.65 to 0.80.

### Acknowledgements

The MIT Hyperloop Team was fortunate to have an array of sponsors, who generously provided advice and funding for this project; their support is hereby acknowledged. For this work in particular, Siemens Product Lifecycle Management is thanked for sponsoring the use of STAR-CCM+. Additionally, we would like to thank SpaceX for organizing and hosting this competition. We would also like to express our gratitude to Mark Drela for his initial advice on the aerodynamic design, allowing the use of MTFLOW, and adapting MTFLOW to handle blunt trailing edges better. Finally, this engineering project's successful outcome was the result of a massive team effort by the MIT Hyperloop Team, consisting of 35 team members across the Mechanical Engineering, Aeronautical and Astronautical Engineering, and Electrical Engineering and Computer Science departments, as well as the Sloan School of Management. This work could not have been completed without their contribution.

### References

- [1] "Hyperloop Alpha," SpaceX, Hawthorne, CA, 2013, [http://www.spacex.com/sites/spacex/files/hyperloop\\_alpha-20130812.pdf](http://www.spacex.com/sites/spacex/files/hyperloop_alpha-20130812.pdf) [retrieved 01 July 2015].
- [2] "Pre-Feasibility Study Stockholm-Helsinki Using Hyperloop One Technology-Short Summary," KPMG AB, Stockholm, Sweden, July 2016, <https://home.kpmg.com/content/dam/kpmg/pdf/2016/07/fs-links-pre-feasibility-study-summary.pdf>.
- [3] Zimmerman, L., "MIT Students Win First Round of SpaceX Hyperloop Contest," *MIT News*, Feb. 2016, <http://news.mit.edu/2016/mit-students-win-first-round-spacex-hyperloop-contest-0201> [retrieved Oct. 2016].
- [4] Chin, J. C., Gray, J. S., Jones, S. M., and Berton, J. J., "Open-Source Conceptual Sizing Models for the Hyperloop Passenger Pod," *56th AIAA/ASCE/AHS/ASC Structures, Structural Dynamics, and Materials Conference*, AIAA Paper 2015-1587, Jan. 2015. doi:10.2514/6.2015-1587
- [5] Decker, K., Chin, J., Peng, A., Summers, C., Nguyen, G., Oberlander, A., Sakib, G., Sharifrazi, N., Heath, C., and Gray, J. S., et al., "Conceptual Sizing and Feasibility Study for a Magnetic Plane Concept," *55th AIAA Aerospace Sciences Meeting*, AIAA Paper 2017-0221, Jan. 2017. doi:10.2514/6.2017-0221
- [6] Braun, J., Sousa, J., and Pekardan, C., "Aerodynamic Design and Analysis of the Hyperloop," *AIAA Journal*, Vol. 55, No. 12, 2017, pp. 4053–4060. doi:10.2514/6.2017-0221
- [7] Goddard, R. H., "The Limit of Rapid Transit," *Scientific American*, Vol. 101, No. 21, 1909, p. 366.
- [8] Bachelet, E., "Levitating Transmitting Apparatus," U.S. Patent 1,020,942, filed 2 April 1910.
- [9] Salter, R. M., "The Very High Speed Transit System," Tech. Rept. P-4874, RAND Corp., Santa Monica, CA, 1972.
- [10] Kantrowitz, A., and Donaldson, C., "Preliminary Investigation of Supersonic Diffusers," NACA Rept. L5D20, 1945.
- [11] Opgenoord, M. M. J., Merian, C., Mayo, J., Kirschen, P., O'Rourke, C., and Izatt, G., "MIT Hyperloop Final Report," Massachusetts Inst. of Technology, Cambridge, MA, Aug. 2017. doi:10.13140/RG.2.2.21941.58088
- [12] Fink, H., and Hobrecht, C., "Instability of Vehicles Levitated by Eddy Current Repulsion-Case of an Infinitely Long Current Loop," *Journal of Applied Physics*, Vol. 42, No. 9, 1971, pp. 3446–3450. doi:10.1063/1.1660751
- [13] Davis, L., and Wilkie, D. F., "Analysis of Motion of Magnetic Levitation Systems: Implications for High-Speed Vehicles," *Journal of Applied Physics*, Vol. 42, No. 12, 1971, pp. 4779–4793. doi:10.1063/1.1659855
- [14] Knudsen, M., "Die Gesetze der Molekularströmung und der Inneren Reibungsströmung der Gase durch Röhren," *Annalen der Physik*, Vol. 333, No. 1, 1909, pp. 75–130. doi:10.1002/andp.19093330106
- [15] Chen, G., *Nanoscale Energy Transport and Conversion: A Parallel Treatment of Electrons, Molecules, Phonons, and Photons*, Oxford Univ. Press, New York, 2005.
- [16] Drela, M., *A User's Guide to MTFLOW 2.01*, Massachusetts Inst. of Technology, Cambridge, MA, 2010.
- [17] Van Ingen, J. L., "A Suggested Semi-Empirical Method for the Calculation of the Boundary Layer Transition Region," Rept. VTH-74, Technische Hogeschool Delft, Delft, The Netherlands, 1956.
- [18] Smith, A. M. O., and Gamberoni, N., "Transition, Pressure Gradient, and Stability Theory," Rept. ES 26388, Douglas Aircraft Co., El Segundo, CA, 1956.
- [19] Barr, A. H., "Superquadrics and Angle-Preserving Transformations," *IEEE Computer Graphics and Applications*, Vol. 1, No. 1, 1981, pp. 11–23. doi:10.1109/MCG.1981.1673799
- [20] Drela, M., *Flight Vehicle Aerodynamics*, MIT Press, Cambridge, MA, 2014, p. 93, Chap. 5.
- [21] Dodbele, S. S., "Effects of Forebody Geometry on Subsonic Boundary-Layer Stability," Vigyan Research Associates, CR NAS1-17919, Hampton, VA, 1990.
- [22] Achenbach, E., "Experiments on the Flow Past Spheres at Very High Reynolds Numbers," *Journal of Fluid Mechanics*, Vol. 54, No. 3, 1972, pp. 565–575. doi:10.1017/S0022112072000874
- [23] Preston, J. H., "The Minimum Reynolds Number for a Turbulent Boundary Layer and the Selection of a Transition Device," *Journal of Fluid Mechanics*, Vol. 3, No. 4, 1958, pp. 373–384. doi:10.1017/S0022112058000057
- [24] Bearman, P., "On Vortex Shedding from a Circular Cylinder in the Critical Reynolds Number Regime," *Journal of Fluid Mechanics*, Vol. 37, No. 3, 1969, pp. 577–585. doi:10.1017/S0022112069000735
- [25] Menter, F. R., "Zonal Two Equation Turbulence Models for Aerodynamic Flows," *23rd Fluid Dynamics, Plasmadynamics, and Lasers Conference*, AIAA Paper 1993-2906, July 1993. doi:10.2514/6.1993-2906
- [26] Menter, F. R., "Two-Equation Eddy-Viscosity Turbulence Models for Engineering Applications," *AIAA Journal*, Vol. 32, No. 8, 1994, pp. 1598–1605. doi:10.2514/3.12149
- [27] Menter, F., Kuntz, M., and Langtry, R., "Ten Years of Industrial Experience with the SST Turbulence Model," *Proceedings of the 4th International Symposium on Turbulence, Heat and Mass Transfer*, edited by K. Hanjalic, Y. Nagano, and M. J. Tummers, Begell House Inc., Redding, CT, Dec. 2003, pp. 625–632.

M. M. Choudhari  
Associate Editor